Assessment of Carotid Artery Plaque Components With Machine Learning Classification Using Homodyned-K Parametric Maps and Elastograms

Marie-Hélène Roy-Cardinal, François Destrempes, Gilles Soulez, and Guy Cloutier, *Senior Member, IEEE*

***Abstract*— Quantitative ultrasound (QUS) imaging methods, including elastography, echogenicity analysis, and speckle statistical modeling, are available from a single ultrasound (US) radio-frequency data acquisition. Since these US imaging methods provide complementary quantitative tissue information, characterization of carotid artery plaques may gain from their combination. Sixty-six patients with symptomatic ($n = 26$) and asymptomatic ($n = 40$) carotid atherosclerotic plaques were included in the study. Of these, 31 underwent magnetic resonance imaging (MRI) to characterize plaque vulnerability and quantify plaque components. US radio-frequency data sequence acquisitions were performed on all patients and were used to compute noninvasive vascular US elastography and other QUS features. Additional QUS features were computed from three types of images: homodyned-K (HK) parametric maps, Nakagami parametric maps, and log-compressed B-mode images. The following six classification tasks were performed: detection of 1) a small area of lipid; 2) a large area of lipid; 3) a large area of calcification; 4) the presence of a ruptured fibrous cap; 5) differentiation of MRI-based classification of nonvulnerable carotid plaques from neovascularized or vulnerable ones; and 6) confirmation of symptomatic versus asymptomatic patients. Feature selection was first applied to reduce the number of QUS parameters to a maximum of three per classification task. A random forest machine learning algorithm was then used to perform classifications. Areas under receiver-operating curves (AUCs) were computed with a bootstrap method. For all tasks, statistically significant higher AUCs were achieved with features based on elastography, HK parametric maps, and B-mode gray levels, when compared to elastography alone or other QUS alone ($p < 0.001$). For detection of a large area of lipid, the combination yielding the highest AUC (0.90, 95% CI 0.80–0.92, $p < 0.001$) was based on elastography, HK, and B-mode gray-level features. To detect a large area of calcification, the highest AUC (0.95, 95% CI 0.94–0.96, $p < 0.001$) was based on HK and B-mode gray level features. For other tasks, AUCs varied between 0.79 and 0.97. None of the best combinations contained Nakagami features. This study shows the added value of combining different features computed from a single US acquisition with machine learning to characterize carotid artery plaques.**

***Index Terms*— Carotid artery plaque, elastography, homodyned-K distribution, machine learning, quantitative ultrasound (QUS), random forest classification, tissue characterization.**

Manuscript received March 22, 2018; accepted June 22, 2018. Date of publication June 29, 2018; date of current version March 14, 2019. This work was supported in part by the Canadian Institutes of Health Research under Grant PPP-78763, Grant CPG-134748, and Grant CHRP-462240, in part by the Natural Sciences and Engineering Research Council of Canada under Grant STPGP-381136 and Grant DG-138570, and in part by the Department of Radiology, Radio-Oncology and Nuclear Medicine, University of Montreal. *(Corresponding author: Guy Cloutier.)*

M.-H. Roy-Cardinal and F. Destrempes are with the Laboratory of Biorheology and Medical Ultrasonics, University of Montreal Hospital Research Center, Montreal, QC H2X 0A9, Canada.

G. Soulez is with the Department of Radiology, Radio-Oncology and Nuclear Medicine, University of Montreal, Montreal, QC H3T 1J4, Canada, with the Institute of Biomedical Engineering, University of Montreal, Montreal, QC H3T 1J4, Canada, and also with the Department of Radiology, University of Montreal Hospital, Montreal, QC H2L 4M1, Canada.

G. Cloutier is with the Laboratory of Biorheology and Medical Ultrasonics, University of Montreal Hospital Research Center, Montreal, QC H2X 0A9, Canada, with the Department of Radiology, Radio-Oncology and Nuclear Medicine, University of Montreal, Montreal, QC H3T 1J4, Canada, and also with the Institute of Biomedical Engineering, University of Montreal, Montreal, QC H3T 1J4, Canada (e-mail: guy.cloutier@umontreal.ca).

Digital Object Identifier 10.1109/TUFFC.2018.2851846

I. Introduction

STROKE is one of the main causes of long-term disability and is triggered by carotid atherosclerotic plaque rupture in approximately 20% of cases [1]. When an atherosclerotic plaque has a high risk of rupture, it is deemed vulnerable.

Magnetic resonance imaging (MRI) is currently the gold standard for carotid plaque assessment [2]. This imaging modality allows identifying intraplaque hemorrhage, plaque ulceration, plaque neovascularity, fibrous cap thickness, and the presence of a lipid-rich necrotic core or calcification. Some of these plaque characteristics, such as a large lipid core, intraplaque hemorrhage, fibrous cap rupture, and gadolinium contrast enhancement (neovascularization), are associated with symptomatic carotid artery plaques [3]. Asymptomatic patients with carotid plaques identified as high risk with MRI are particularly exposed to future cerebrovascular events [4]. However, MRI is a time constraining and expensive imaging modality. Moreover, protocols allowing high-resolution carotid plaque imaging are mainly used for research purposes and are not widely implemented on commercial MRI scanners [5].

Duplex ultrasound (US) is the first line examination to grade artery stenosis, whereas computed tomography or MRI is used to corroborate stenosis grading and evaluate intracranial and arch extension of atherosclerotic disease before endarterectomy [6]. In addition to stenosis quantification with duplex and color Doppler imaging, US elastography can evaluate biomechanical properties of plaques. Other quantitative US (QUS) imaging methods aiming at quantifying the microstructure

of biological tissues can also be obtained by processing a single US radio-frequency data acquisition. As described next, these US imaging methods may thus provide additional and complementary quantitative tissue information and have been investigated for carotid artery plaque assessment. The underlying hypothesis is that vulnerable plaques differ from nonvulnerable ones in their tissue biomechanical properties, morphology, and composition [7].

The strain (deformation), assessed with MRI elastography, has been found lower in complex carotid artery plaques [American Heart Association (AHA) stages IV to VIII] than in simple ones (AHA stages I to III) [8]. Classification of vulnerable carotid artery plaques based on combined elastography and B-mode US imaging had increased sensitivity, specificity, and accuracy compared with classification based on elastography or B-mode imaging alone [9]. US strain indices were also correlated with cognitive impairment scores in patients who underwent carotid endarterectomy of plaques with high-grade stenosis [10]. Texture analysis applied on US strain images of MRI-detected vulnerable versus stable carotid artery plaques revealed higher local deformation magnitude and deformation pattern complexity in vulnerable plaques [11]. US strain imaging was also able to differentiate between fibrous and atheromatous carotid artery plaques using high strain index and area of the inner plaque layer [12]. A recent review of carotid artery stiffness measurement methods reported that the presence of plaque and the occurrence of incident stroke are associated with increased vessel stiffness [13].

Besides strain imaging, QUS has been investigated in the context of carotid artery plaque assessment, and echolucent plaques were correlated with an increased risk of stroke [14]. Lipid-like echogenicity in carotid artery plaques was also associated with higher plaque instability in asymptomatic patients [15]. Moreover, ultrasonic plaque features were associated with unstable plaques validated with histology [16], and were included with clinical information in a cerebrovascular risk stratification model for asymptomatic subjects [17]. Recently, gray-scale US features were associated with histopathology markers of carotid plaque vulnerability [18]. Even though carotid plaque echolucency is associated with a high risk of stroke, a recent review suggested that this feature alone is not a powerful enough risk factor to select asymptomatic stenotic patients for surgery [19]. First- and second-order textural features, based on gray-level co-occurrence matrix, were correlated with visual classification and histological examination of carotid plaques [20]. In [21] and [22], global measures of echogenicity and texture were proposed to characterize the 3-D echo morphology of carotid plaques. Parametric echogenicity maps based on Nakagami m-parameter were first introduced in the pioneer work of Shankar *et al.* [23]. This method was then further refined in [24], based on a coarse-to-fine approach. In [25], another statistical method based on discrete Fréchet distance between bimodal gamma distributions was proposed for the classification of echolucent carotid plaques.

In previous studies [26] and [27], we have proposed elastography parameters to characterize tissue deformation of carotid artery plaques. We have also developed statistical QUS parameters based on homodyned-K (HK) modeling that were related to tissue microstructure in the context of aggregated red blood cells [28] and breast lesions [29]. In this study, we hypothesize that the combination of elastography with other QUS features in a machine learning scheme can characterize plaque components with a higher accuracy than elastography or other QUS features alone. Specifically, as a primary endpoint, noninvasive vascular US elastography (NIVE), HK, Nakagami, and echogenicity features were combined in a random forest classifier to evaluate MRI-determined amount of lipid and calcified plaque components, and to detect a ruptured fibrous cap. As a secondary endpoint, the proposed method was also applied to differentiate MRI-categorized nonvulnerable plaques from neovascularized or vulnerable ones, and to study patient symptomatology.

II. Methodology

A. Database

Atherosclerotic plaques of the internal left or right carotid artery (with $>50\%$ stenosis) were assessed in this study. A total of 66 patients were recruited: 40 patients presented carotid artery plaques that were not associated with neurologic symptoms; 26 patients had a stroke or transient ischemic event that was related to the studied plaque. For patients with neurologic symptoms, the ipsilateral carotid side was chosen, whereas the side with the most severe stenosis was considered for asymptomatic subjects. This study has received institutional review board approval. Written informed consent was obtained from all participants. This population has been studied in [26], [27], and [30].

B. US Imaging

Plaques of internal carotid arteries were scanned in longitudinal view by an experienced radiologist with an ES500RP system (Ultrasonix, Vancouver, Canada), and cine loops of raw US radio-frequency data sampled at 20 MHz were recorded. Acquisitions were performed with a linear array transducer (L14-5/38) characterized by a 7.2-MHz center frequency. The frame rate ranged between 19 and 25 frames/s and data were recorded for approximately 10 s.

The carotid artery plaque contours in each image of the US cine loops were delineated using a semiautomatic segmentation method [31]. All segmentations were verified by an experienced radiologist. Elastograms, HK and Nakagami statistical parametric maps, and echogenicity parameters were computed from acquired RF data within the segmented carotid artery plaque region. Reconstructed B-mode sequences were used for statistical parametric maps and echogenicity measures.

C. MRI Imaging

The study was divided in two phases and subjects from the second subgroup of 31 participants had an MRI examination (T2-weighted imaging, proton-density-weighted imaging, and unenhanced and contrast-enhanced T1-weighted imaging) [26], [27]. MRI cross-sectional images of the carotid artery were obtained with a dedicated surface coil. Nine symptomatic

carotid artery plaques were included in the MRI substudy; the remaining 22 plaques were asymptomatic. Images were acquired 1 cm below to 3 cm above the carotid artery bifurcation with a voxel size of $0.6 \times 0.5 \times 3$ mm^3. Details on MRI acquisitions and image analysis can be found in [27]. MRI images were used as a reference method to assess the lipid and calcium contents of each plaque, the presence of intraplaque hemorrhage and neovasculature, and status of the fibrous cap (ruptured, thin, or nonruptured). A plaque was categorized as vulnerable if it contained either a ruptured fibrous cap, a intraplaque hemorrhage, neovasculature, or a thin fibrous cap with a large lipid core (at least one cross-sectional lipid area above 25%).

Computer-aided manual segmentation of plaque components was performed on MRI images with specialized software (QPlaque MR 1.0.16, Medis, The Netherlands) [32]. Lumen, vessel, and plaque component contours were traced on each cross-sectional image to provide area measurements.

D. Elastography Parametric Maps and Selected Biomarkers

Axial strains, axial shear strains, and axial and lateral translations of a carotid artery plaque were measured locally within small measurement windows and averaged over the segmented plaque area. Mechanical motions were induced by the natural artery pulsation. Axial motion parameters are in the US beam direction, whereas lateral ones are perpendicular to it. Strain represents either compression or dilation of plaque tissue components, whereas shear strain can be viewed as an angular deformation or change in shape of tissue components, occurring during the cardiac cycle. Translations correspond to rigid motion of plaque tissue components. These 2-D deformation maps were computed with a NIVE method [33], [34] implemented and integrated into imaging software (Visual, Object Research Systems, Montreal, QC, Canada).

Time-varying curves of these elastograms averaged over the whole segmented plaque were plotted over time to produce instantaneous strain, shear strain, and translation curves. The instantaneous terminology refers to estimates computed from pairs of consecutive frames in the cine loop. Because ECG gating was not available, cardiac cycles were manually identified on these curves. Instantaneous curves were cumulated over time for each selected cardiac cycle to obtain cumulative parameter computations. To emphasize localized high motions presumably attributed to lipid pool deformation of vulnerable plaques, instantaneous and cumulated curves were also computed by considering only pixels with highest magnitude in elastograms, as in [27]. In this case, a threshold was used to select the 25% highest strain, shear strain, and translation values on each frame.

Specific biomarkers were then extracted from axial strain, axial shear strain, axial translation, and lateral translation curves (with or without thresholding). Otherwise specified, the maximum of these biomarkers was computed from instantaneous measures. These features are: maximum and cumulated axial strains (MaxAS and CAS), maximum and cumulated absolute shear strains (Max|ShS| and C|ShS|), cumulated axial translation (CAT), cumulated lateral translation (CLT), and the CAS to CAT ratio [27]. Feature values were averaged over all complete cardiac cycles of a cine loop. A total of 14 elastogram features were thus available as input in the classification model. In detail, for MRI-determined plaque component and vulnerability classification tasks, only thresholded translations and axial strain features, and unthresholded shear strain features were used to avoid statistical redundancy of parameters, as done in [27]. On the other hand, for patients' symptomatology classification, only unthresholded parameters were used, as in [30]. Thus, for each task, 7 out of 14 elastography features were used in the input vector, according to the task.

E. Other QUS Parametric Maps and Selected Biomarkers

Prior to estimation of HK parameters, pixels within the previously delineated plaque were classified with an unsupervised method into a maximum of three labels, since carotid artery plaques may present three distinct main constituents (i.e., lipid, calcium, and fibrosis). Thus, a segmentation algorithm based on a Markov random field model [35] was used with each label representing a distinct probability density function of the echo envelope (without log compression) of the radio-frequency data within the plaque. The probability density functions for this task were modeled as Nakagami distributions, as done previously for US echo-envelope characterization [36], and were estimated with the expectation–maximization algorithm adapted to US images [37]. Nakagami distributions were estimated for each cine loop and the pixels classification algorithm was applied to each image of the US cine loop. An example of a B-mode image of a segmented carotid artery plaque is displayed in Fig. 1(a). Fig. 1(b) shows pixel labeling (classification) within the plaque; in this case, two classes of pixels were found by the algorithm based on Nakagami modeling.

Based on the assumption that the echo envelope is distributed locally according to a single HK, ε, σ, and α defining this distribution were estimated locally based on log-moment statistics [38]. HK estimations were performed within local sliding windows of size 2×2 mm^2 (52×13 pixels^2), with center position sweeping the segmented plaque region with a step of four pixels axially and one pixel laterally. To estimate parameters from a single HK distribution, only pixels corresponding to the same (Nakagami) probability density function of the echo envelope (i.e., with the same label as that of the center of the sliding window) were used [28]; Fig. 1(c) presents an estimation window for HK (and Nakagami m-parameter, see below), and those pixels with the same label as the center pixel of the estimation window are shown. (Other pixels correspond to the B-mode image of the plaque.) The HK parameters yielded three metrics considered in [39]: the mean intensity $\mu = \varepsilon^2 + 2\sigma^2\alpha$, the reciprocal $1/\alpha$, and the coherent-to-diffuse signals ratio k. The mean intensity μ is akin to B-mode echogenicity; we actually considered its normalization μ_n by the maximal intensity within the plaque. α is the scatterer clustering parameter; a greater value indicates a greater acoustical homogeneity within the scattering medium. It was more convenient numerically to

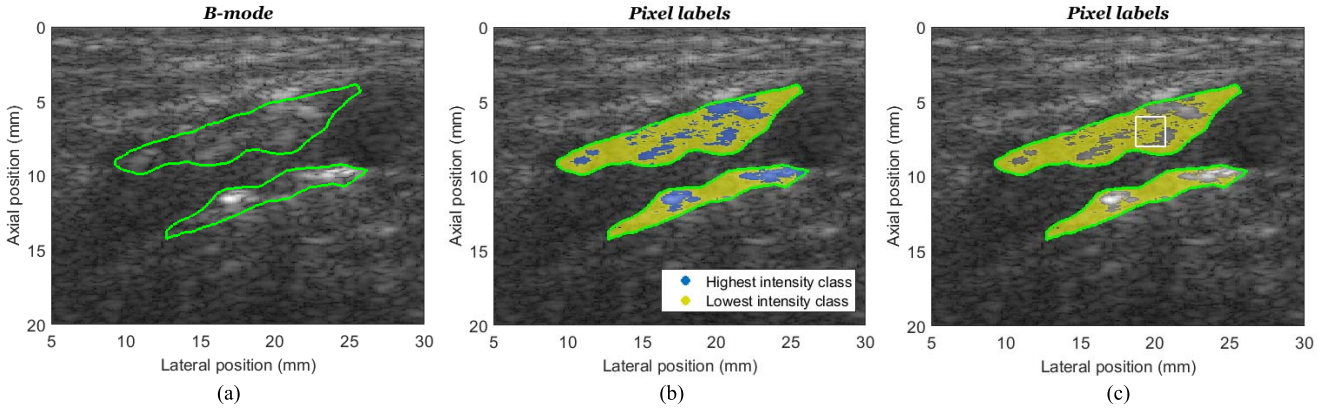

Fig. 1. (a) Example of a segmented carotid artery plaque superimposed on a reconstructed B-mode image with a pixel size of 38.5×149.6 μm^2. Segmentation was performed on radio-frequency-based reconstructed B-mode images but under the visual guidance of a second scan performed with an HDI 5000 system (color duplex mode, L7-4 probe, Philips Healthcare). (b) Plaque pixel labeling into two classes. (c) Schematic representation of a clipped sliding estimation window of 2×2 mm^2 (white rectangle). The pixels with same label as the center pixel of the estimation window (corresponding to a single probability density function) are represented in yellow; the other label is not displayed. QUS HK and Nakagami parameters associated with the center pixel of the window were estimated using only the yellow pixels inside the window.

consider the reciprocal of α, rather than α itself, since a perfectly homogenous scattering medium would have an infinite value, whereas $1/\alpha = 0$. We also selected a fourth parameter, the diffuse-to-total signal powers ratio $1/(\kappa + 1)$, considered in [28]. A greater value of k or κ reveals the presence of a coherent echo component, due possibly to periodic alignment of scatterers or specular reflection [39], or highly structured spatial organization of scatterers [28]. In contrast, a low value of these two parameters is an indicator of randomly positioned scatterers within the scattering medium.

Based on this procedure, four HK parametric maps [μ_n, $1/\alpha$, k, $1/(\kappa + 1)$] were produced on each frame of a US cine loop. This approach of estimating echo envelope statistical parameters on clipped sliding windows was also applied to obtain Nakagami m parametric maps. Indeed, the label maps, previously computed for HK parameter estimation, were also used to select pixels corresponding to a single probability density function of the echo envelope within each window, for Nakagami m-parameter estimation. Biomarkers could then be extracted from the above five parametric images. Specifically, mean and interquartile range (IQR) of each map were computed for a total of 10 QUS features. Values were averaged out over all frames of a cine loop. QUS computation was performed using C++ and MATLAB R2010 (MathWorks, Natick, MA, USA) computer programs.

In addition, four classical features based solely on echogenicity were also computed [17]. They were obtained from gray-level intensity of reconstructed compressed B-mode images, after normalization of gray levels between 0 and 190, as proposed in [17]. The value "0"corresponded to the lowest gray level in a 3-mm-thick region adjacent to the plaque in the lumen, and the value "190" was assigned to the highest gray level in a 3-mm-thick region adjacent to the plaque in the adventitia and surrounding tissues. The 3-mm regions were bounded by the lumen and plaque contours and by these same contours shifted axially (by 3 mm) toward the lumen and adventitia, respectively. Computed features were the mean gray level (MGL), coefficient of variation of gray levels (CVGLs), percentage of low intensity gray levels (PLGLs) (i.e., <75), and percentage of high intensity gray levels (PHGLs) (i.e., ≥150). These four echogenicity features were computed over all carotid artery plaque pixels of a cine loop, for a total of 14 QUS features, besides elastogram features. All features considered in the selection process of the machine learning strategy are summarized in Table I.

TABLE I

LIST OF FEATURES EXTRACTED FROM QUS AND ELASTOGRAM PARAMETRIC MAPS. FOR QUS, THE TYPE OF EACH PARAMETER IS INDICATED IN ITALIC (HK—HOMODYNED-K; NAKAGAMI; AND ECHOGENICITY)

QUS features	Description	Elastogram features	Description
μ_n Avg	Average of μ_n *(HK)*	MaxAS	Maximal axial strain (%)
$1/\alpha$ Avg	Average of *1/α (HK)*	CAS	Cumulated axial strain (%)
k Avg	Average of *k (HK)*	Max|ShS|	Maximal shear strain magnitude (%)
$1/(\kappa+1)$ Avg	Average of *1/(κ+1) (HK)*	C|ShS|	Cumulated shear strain magnitude (%)
μ_n IQR	Inter-quartile range (IQR) of μ_n *(HK)*	CAT	Cumulated axial translation (mm)
$1/\alpha$ IQR	IQR of *1/α (HK)*	CLT	Cumulated lateral translation (mm)
k IQR	IQR of *k (HK)*	CASCAT	Cumulated axial strain to axial translation ratio
$1/(\kappa+1)$ IQR	IQR of $1/(\kappa+1)$ *(HK)*	MaxAS_T	Thresholded maximal axial strain (%)
m Avg	Average of m *(Nakagami)*	CAS_T	Thresholded cumulated axial strain (%)
m IQR	IQR of m *(Nakagami)*	$\text{Max\|ShS\|}_\text{T}$	Thresholded maximal shear strain magnitude (%)
MGL	Mean gray level value (0-190 intensity scale) *(echogenicity)*	$\text{C\|ShS\|}_\text{T}$	Thresholded cumulated shear strain magnitude (%)
CVGL	Coefficient of variation of gray level value *(echogenicity)*	CAT_T	Thresholded cumulated axial translation (mm)
PLGL	Percentage of low gray level value *(echogenicity)*	CLT_T	Thresholded cumulated lateral translation (mm)
PHGL	Percentage of high gray level value *(echogenicity)*	CASCAT_T	Thresholded cumulated axial strain to axial translation ratio

F. Random Forest Classification

A random forest classifier [40], [41] consists of multiple decision trees, each tree selecting a class according to an input vector of features. The random forest classifier then outputs the class that is attributed by the individual decision trees, with highest frequency. Random forests are not prone to overfitting and have a small number of parameters to adjust during training [40].

Random forest classification was thus used to assess the presence of plaque vulnerability, lipid content, calcium content, fibrous cap status, and to confirm the relation with symptomology (i.e., to differentiate patients that had a stroke or transient ischemic event from asymptomatic ones). Lipid and calcium contents were separated into categories: two classes for lipid and one for calcium. Six classification tasks were thus defined. All tests were performed with package "RandomForest" version 4.6-12 for R [42].

Overall, 14 elastography and 14 B-mode QUS features were chosen as potential input for classification. The first step of the classification process was to select a limited number of features to reduce data dimensionality, and consequently decrease the training time and the generalization error (due to less overfitting). Feature selection was based on the G-mean $= \sqrt{\text{sensitivity} \times \text{specificity}}$. This index is recommended as an evaluation measure in the case of imbalanced data [43]. The G-mean was evaluated for all possible combinations of 3 or less features among the 28 proposed ones. The 40 combinations of features with highest G-mean values were selected for training and testing classifiers. Receiver-operating characteristic (ROC) curves were generated for each of these 40 selected feature combinations, as described as follows. For the feature selection step, the number of trees in random forests was set to 3000.

To evaluate classification based on retained combinations of features, a bootstrap technique was chosen due to the small data set (i.e., $n = 31$ for the subgroup with available MRI analysis, or $n = 66$ for the entire database). The "0.632+" bootstrap method evaluates the training and cross-validation errors, and then weights them so as to predict the generalization error [44]. The training error typically underestimates the generalization error, while the latter is typically overestimated with the leave-one-out cross-validation used in statistical learning [45, ch. 7]. This bootstrap method was selected because it showed low bias and mean squared error for classification tree schemes applied to small data sets of 40 and 80 samples, in the case of low data dimensionality (less than 10 features) [46]. Stratified "0.632+" bootstrap samples were generated to construct ROC curves. The sampling proportion of each class varied from 0 to 1, with a step of 1/39, for a total of 40 strata. For each stratification step of ROC curves, 1000 bootstrap samples were drawn, and classification sensitivity and specificity were evaluated. With such cross-validation method, each test set consists of patients data excluded from the bootstrap sample. The area under the ROC curve (AUC) was computed with the trapezoidal method to evaluate the accuracy of tested classification schemes. Finally, since the size of each random forest tree can be limited to a maximum number of terminal nodes (MTNs), this parameter was used to achieve the lowest complexity of classifiers. ROC curves were thus constructed for each MTN varying between 2 and 20 and increasing by steps of 2; classifiers with the highest ROC AUC were selected. In the case of a tie in ROC values, the lowest MTN was chosen. The AUC could then be computed for each of these 40 ROC curves. The combination of features with maximal AUC was reported in this paper. For ROC computations, the number of trees in random forests was set to 1000.

TABLE II
POPULATION CHARACTERISTICS; VALUES ARE MEAN ± SD

Clinical parameters	All subjects (N=66)	MRI subgroup (N=31)	Non MRI subgroup (N=35)	p-value
Male (number) [a]	47 (71%)	22 (71%)	25 (71%)	0.817
Age [b]	70 ± 8	69 ± 8	71 ± 9	0.456
Stenosis (%)[b]	73 ± 14	73 ± 12	74 ± 15	0.620
SBP (mm Hg) [b]	135 ± 16	134±17	136 ± 14	0.503
DBP (mm Hg) [b]	71 ± 10	69 ±10	73 ± 10	0.116

SBP: systolic blood pressure, DBP: diastolic blood pressure.
[a] Pearson's Chi Square test with Yates correction for continuity.
[b] Student t-test.

G. Other Statistical Analyses

Other statistical analyses were also performed using *R* statistical software (R Foundation, Vienna, Austria) and MATLAB 2010 (The MathWorks Inc., Natick, MA, USA). Correlation between elastogram components and B-mode QUS parametric maps were determined to investigate any coregistered spatial relation between these two different types of information. Pixel-to-pixel correlation of each QUS map μ_n, $1/\alpha$, k, $1/(\kappa + 1)$, or m with each elastogram map of axial strain, axial shear strain, axial and lateral translations were computed. Relationships (correlations) between echogenicity (MGL, CVGL, PLGL, PHGL) and elastograms could not be established because echogenicity metrics were determined from all pixels of the cine loop; no images were produced. Correlation coefficients were assessed on each frame of a US cine loop. The average and maximal correlation coefficients over all frames of the cine loop were then computed. Mean values of these quantities over all subjects are reported. Confidence intervals (CI, confidence level of 95%) for the ROC AUC measurements were estimated with the nonparametric jackknife method [47]. The Wilcoxon signed rank test was used to detect statistically significant difference between ROC AUCs.

III. RESULTS

A. Database

Following MRI imaging, 12 plaques were categorized as nonvulnerable and 19 as vulnerable or neovascularized. Lipid was found in 17 plaques and calcium in 27; there were five cases of ruptured fibrous cap and two cases of intraplaque hemorrhage. Table II reports clinical parameters of the population and the MRI and non-MRI subgroups. Supplementary clinical parameters derived from clinical and MRI examinations can be found in [27, Table 1] and [30, Table 1].

TABLE III
CORRELATION COEFFICIENTS (R) BETWEEN ELASTOGRAPHY AND HOMODYNED-K PARAMETRIC MAPS

	μ_n			$1/\alpha$			k			$1/(\kappa+1)$		
	Avg ($\|R\|$)	Max ($\|R\|$)	p	Avg ($\|R\|$)	Max ($\|R\|$)	p	Avg ($\|R\|$)	Max ($\|R\|$)	p	Avg ($\|R\|$)	Max ($\|R\|$)	p
Axial strain	0.14	0.44	**0.044**	0.10	0.34	0.068	0.14	0.43	**0.049**	0.13	0.40	0.051
Axial shear strain	0.16	0.47	**0.040**	0.11	0.36	0.061	0.16	0.50	**0.039**	0.15	0.46	**0.045**
Axial translation	0.17	0.47	**0.035**	0.11	0.38	0.061	0.17	0.51	**0.038**	0.15	0.47	**0.043**
Lateral translation	0.14	0.48	**0.048**	0.10	0.35	0.073	0.14	0.46	**0.049**	0.12	0.42	0.054

Avg($|R|$): for each plaque, absolute value of the correlation coefficient between parametric maps, averaged over all frames of a cine-loop (n=66 subjects).
Max($|R|$): for each plaque, maximum absolute value of the correlation coefficient between parametric maps, over all frames of a cine-loop (n=66 subjects).

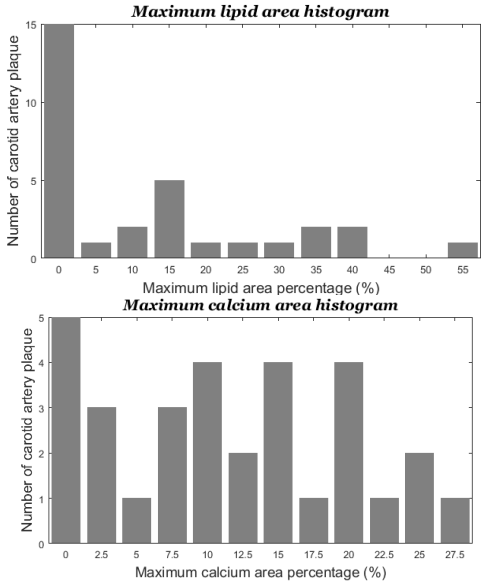

Fig. 2. Histograms of maximum lipid and calcium areas in carotid artery plaques. Lipid and calcium areas were measured from MRI 3-D examinations.

Fig. 2 shows the histogram of maximum lipid and calcium areas. Thresholds to categorize maximum lipid and calcium areas were determined based on these histograms. Two thresholds of 10% and 25% were thus chosen for lipid content, resulting in 15 and 7 plaques, respectively, having a maximum lipid area (over several MRI slices of a volume) greater than 10% and 25%, respectively. A single threshold was chosen for calcium, yielding 18 plaques with a maximum calcium area greater than 10%. Classification based on the presence of intraplaque hemorrhage was not attempted due to a sample size of two.

Examples of parametric maps that were used to compute classification features are shown for a carotid artery plaque in Figs. 3–5 (HK parameters in Fig. 3, Nakagami m statistics in Fig. 4, and cumulated elastograms in Fig. 5). As mentioned earlier, the average and IQR of the parametric maps in Figs. 3 and 4 were computed as HK and Nakagami features (see Table I). Cumulated and thresholded cumulated elastography features were computed from elastograms, as displayed in Fig. 5. Recall that maximum axial strain and axial shear strain features were computed from instantaneous elastograms (not shown).

TABLE IV
CORRELATION COEFFICIENTS (R) BETWEEN ELASTOGRAPHY AND NAKAGAMI ECHO-ENVELOPE STATISTICS m PARAMETRIC MAPS

	m		
	Avg($\|R\|$)	Max($\|R\|$)	p
Axial strain	0.11	0.37	0.057
Axial shear strain	0.14	0.43	**0.049**
Axial translation	0.14	0.45	**0.046**
Lateral translation	0.12	0.42	0.060

See Table 2 for the definition of parameters.

Pixel-to-Pixel Correlation Between Elastograms and B-Mode-Based QUS Statistical Parametric Maps: Correlation coefficients between elastograms and HK parametric maps for the whole database are shown in Table III. Instantaneous elastogram components were correlated with HK parametric maps. Statistically significant correlation coefficients were found between elastography and μ_n, k, and $1/(\kappa + 1)$ parametric maps; however, average correlation values were low. Parameter $1/\alpha$ had no coregistered spatial correspondence.

Table IV shows correlation coefficients between instantaneous elastogram and Nakagami echo-envelope statistics m parametric maps. Statistically significant correlations were found with the axial shear strain and axial translation. Again, average correlation coefficients were low.

B. Classification Results

Six classification tasks were defined: detection of: 1) a small area of lipid; 2) a large area of lipid; 3) a large area of calcification; 4) presence of a ruptured fibrous cap; 5) differentiation of nonvulnerable carotid plaques from neovascularized or vulnerable ones; and 6) differentiation of symptomatic from asymptomatic patients. A schematic representation of a random forest that was used to detect a large area of calcification is shown in Fig. 6. To evaluate the added value of combining elastography with B-mode QUS features, different sets of inputs were used for each classification task: 1) elastography, HK, and B-mode gray-level features; 2) elastography, Nakagami, and B-mode gray level features; 3) elastography features alone; 4) HK and B-mode gray-level

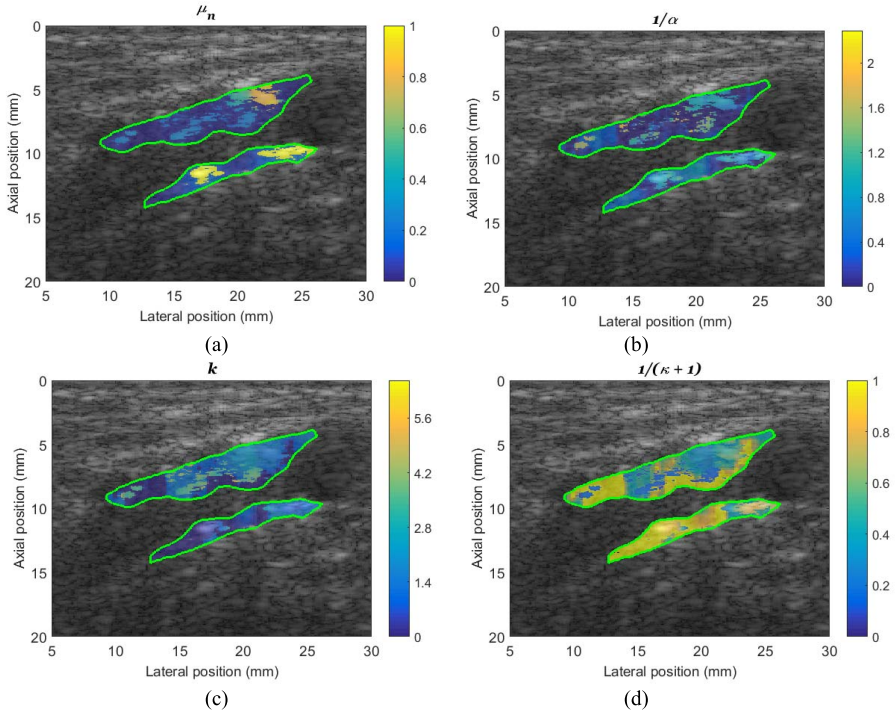

Fig. 3. Examples of HK parametric images of a plaque on the near and far walls of the carotid artery superimposed on a longitudinal B-mode image. (a) Parametric map of the mean intensity μ_n. (b) $1/\alpha$ parametric map (in logarithmic scale)—a lower value of $1/\alpha$ indicates a greater acoustical homogeneity within the plaque. (c) k parametric map. (d) $1/(\kappa+1)$ parametric map—a greater value of k or κ reveals the presence of a coherent component. μ_n, α, k and κ are dimensionless.

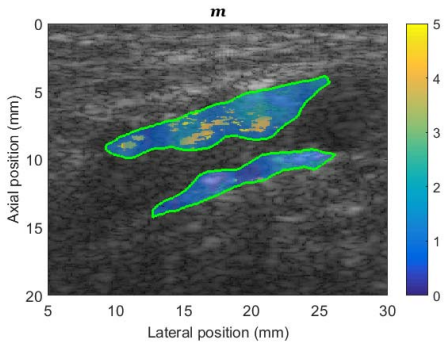

Fig. 4. Example of QUS Nakagami m parametric map of a plaque on the near and far walls of the carotid artery superimposed on a longitudinal B-mode image. m is dimensionless.

features; and 5) Nakagami and B-mode gray level features. For each task and each set of inputs, 40 combinations of features were selected and their ROC curves were constructed; the ROC curve with the highest AUC was kept.

Table V shows results of the six classification tasks and five sets of inputs. For each classification task, the statistically significant highest AUC is marked in bold. Gold standard was established with MRI imaging for the first five tasks ($n = 31$). The gold standard for the last task was based on patient symptoms ($n = 66$).

IV. Discussion

In this study, elastography and QUS were combined to detect plaque components such as lipid, calcium, and ruptured fibrous cap, and to identify vulnerable and symptomatic carotid artery plaques. These tasks were performed with random forest machine learning classifications. The goal was to evaluate the classification gain associated with the combination of different QUS features rather than to identify precise features to be used for carotid plaque characterization, as this objective would require larger data sets.

To identify possible correspondence between QUS cellular metrics and plaque mechanical properties, pixel-to-pixel correlations were computed between all parametric images of acquired US cine loops. This task also aimed at identifying possible redundant information because it is preferred in machine learning to use uncorrelated features [48]. Statistically significant associations were found as listed in Tables III and IV. However, the highest statistically significant correlation coefficient was 0.17 on average, thus indicating low redundancy. All parametric maps were hence kept in this study.

Feature selection was performed before random forest classification, due to a high number of features compared to the data set size. The maximum number of retained features was empirically set to 3; combinations of four features have also been tested using the same feature selection method but they resulted in lower AUCs (data not shown). Fig. 7 shows the training and generalization AUC-ROC with increasing number of features in the random forest for a given classification task (maximum calcium area $\geq$ 10%). As expected, the training AUCs increase and remain high with an increasing number of features, while the generalization AUCs (computed with

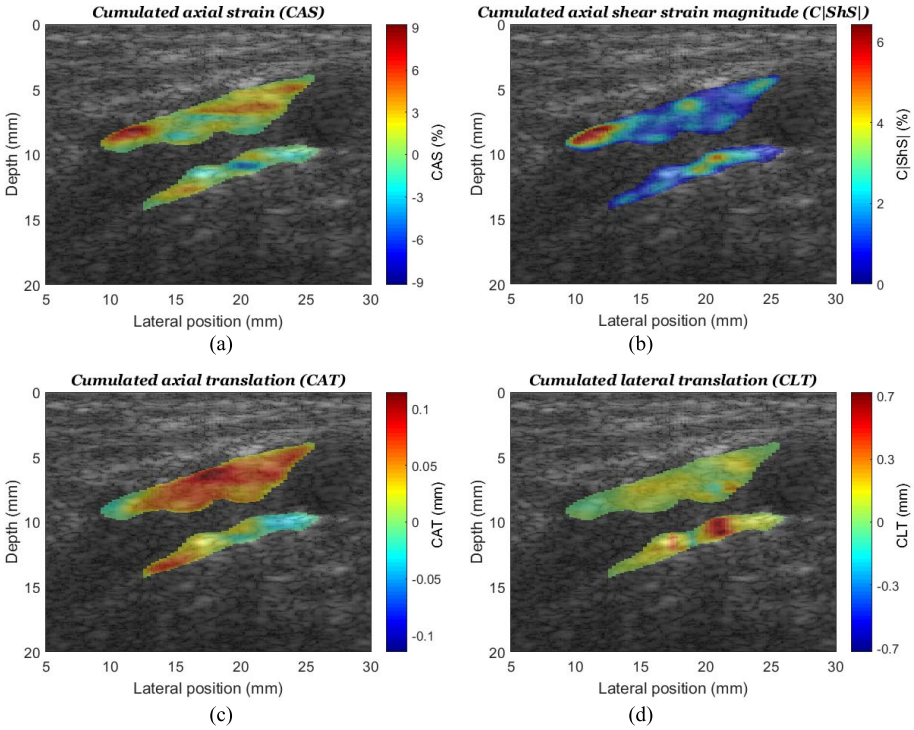

Fig. 5. Examples of elastograms of a plaque on the near and far walls of the carotid artery superimposed on a longitudinal B-mode image. (a) CAS (%). (b) Cumulated axial shear strain magnitude (%). (c) CAT (mm). (d) CLT (mm). Images were cumulated during the diastolic phase of the cardiac cycle.

TABLE V

CLASSIFICATION RESULTS TO DETECT: 1) A MAXIMUM LIPID AREA ≥ 10%; 2) A MAXIMUM LIPID AREA ≥ 25%; 3) A MAXIMUM CALCIUM AREA ≥ 10%; 4) THE PRESENCE OF A RUPTURED FIBROUS CAP; 5) VULNERABLE OR NEOVASCULARIZED CAROTID ARTERY PLAQUES; AND 6) SYMPTOMATIC CAROTID ARTERY PLAQUES

	Lipid area ≥ 10% (15 of 31)	**Lipid area ≥ 25% (7 of 31)**	**Calcium area ≥ 10% (18 of 31)**	**Ruptured fibrous cap (5 of 31)**	**Plaque vulnerability (19 of 31)**	**Presence of symptoms (22 of 66)**
Elasto + *HK* + *echogenicity*	**0.79 [0.77-0.83]** Max|ShS| + PHGL + MGL	**0.90 [0.80-0.92]** Max|ShS| + MGL + *k* Avg	**0.95 [0.94-0.96]** $CASCAT_T$ + PLGL + 1/α IQR	**0.97 [0.95-0.98]** $MaxAS_T$ + PLGL + 1/(κ+1) IQR	**0.91 [0.89-0.93]** CLT_T + CVGL + 1/(κ+1) Avg	**0.83 [0.81-0.84]** Max|ShS| + MaxAS + CVGL
Elasto + *Nakagami* + *echogenicity*	**0.79 [0.77-0.82]** (p=1.00) CAS_T + Max|ShS| + PHGL	0.89 [0.79-0.90] (p<0.001) Max|ShS| + PHGL + *m* IQR	0.90 [0.89-0.93] (p<0.001) CLT_T + PLGL + MGL	**0.97 [0.95-0.98]** (NA) $MaxAS_T$ + PLGL	**0.90 [0.89-0.92]** (p=0.26) $MaxAS_T$ + CLT_T + CVGL	**0.83 [0.81-0.84]** Max|ShS| + MaxAS + CVGL
Elasto only	0.67 [0.56-0.68] (p<0.001) $MaxAS_T$ + CLT_T	0.88 [0.85-0.91] (p<0.001) $CASCAT_T$ + Max|ShS|	0.78 [0.74-0.80] (p<0.001) $MaxAS_T$ + CLT_T	0.89 [0.87-0.91] (p<0.001) $MaxAS_T$ + CAT_T	0.86 [0.84-0.89] (p<0.001) CAT_T + CLT_T + $CASCAT_T$	0.79 [0.78-0.82] (p<0.001) Max|ShS| + C|ShS| + MaxAS
HK + *echogenicity*	0.78 [0.76-0.82] (p=0.022) MGL + CVGL + PHGL	0.83 [0.81-0.83] (p<0.001) PHGL + 1/α Avg	0.94 [0.86-0.95] (p<0.001) PLGL + 1/α IQR + 1/α Avg	0.92 [0.89-0.95] (p<0.001) PLGL + PHGL + *k* IQR	0.80 [0.77-0.84] (p<0.001) CVGL + PHGL	0.69 [0.61-0.70] (p<0.001) MGL + μ_n IQR + μ_n Avg
Nakagami + *echogenicity*	0.78 [0.76-0.82] (p=0.020) MGL + PHGL	0.84 [0.81-0.88] (p<0.001) PHGL + *m* Avg	0.89 [0.88-0.91] (p<0.001) PLGL + PHGL + *m* IQR	0.92 [0.89-0.95] (p<0.001) PLGL + PHGL	0.80 [0.77-0.84] (p<0.001) CVGL + PHGL	0.67 [0.66-0.69] (p<0.001) PHGL + *m* Avg

AUCs are shown with 95% confidence intervals.

Sets of input features for training were: *Elasto* for elastogram features; *HK* for homodyned-K parameters, *Nakagami* parameters; and *echogenicity* for B-mode gray level features. The feature combination that resulted in the highest AUC is shown with feature names given in Table 1.

For each of these tasks, the AUC in bold is the highest for a given task (*i.e.*, same column); p-values are for multiple comparisons with the highest AUC (for a given task) using Wilcoxon rank sum tests, after Holm–Bonferroni correction; there is no p-value for the highest AUC.

bootstraps) reach a maximum with three features. In view of the sample size, overfitting could explain lower AUCs for classifications with more than three features. We avoided overfitting conditions in this study. However, with a larger database, combinations of more than three features would certainly be relevant.

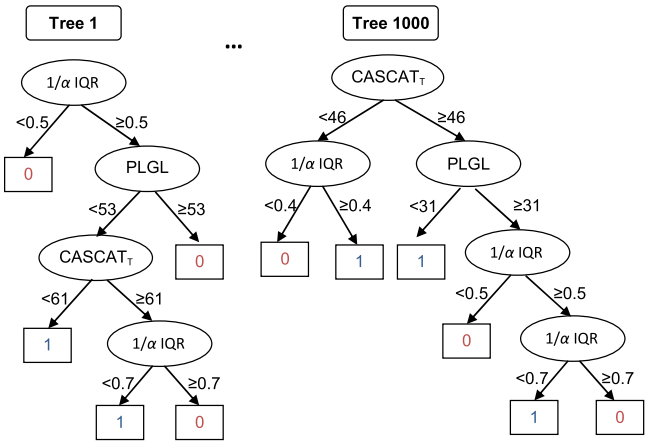

Fig. 6. Schematic representation of a random forest to detect a large area of calcification. The first and last trees are shown. The final decision is 0 (negative) or 1 (positive).

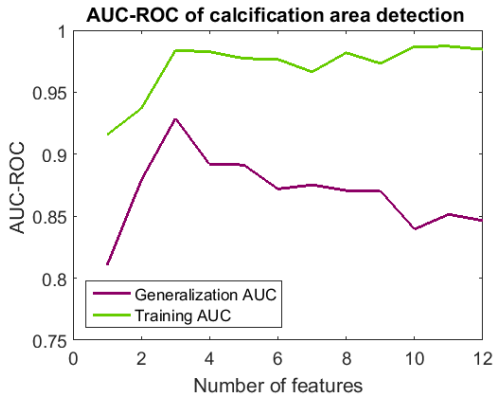

Fig. 7. Training and generalization AUC-ROC for different number of features in the random forest. AUC-ROC computed for the classification task to detect a large area of calcification.

Plaque components have been previously investigated as predictors of cardiovascular events. They provide stroke risk stratification in patients [2]. A systematic literature review has shown that the presence on carotid plaque MRI of a thin/ruptured fibrous cap, a lipid-rich necrotic core, and intraplaque hemorrhage are associated with increased risk of future stroke or transient ischemic attack [49]. Moreover, carotid artery plaque fibrous cap status and lipid content were strongly associated with cardiovascular events (myocardial infarction, ischemic stroke, acute coronary syndrome, coronary revascularization, and cerebrovascular revascularization) [50]. Calcium is also known to be a stabilizing component of a plaque [51] but large calcification volume was, however, associated with intraplaque hemorrhage but less lipid content [52].

AUCs of all classification tasks with different sets of input features were reported in Table V. In all cases, statistically significant higher AUCs ($p < 0.001$) were achieved with a combination of features among elastography, HK, and B-mode gray-level ones (Table V, lines 1 and 2), when compared to elastography alone (Table V, line 3) or QUS alone (Table V, lines 4 and 5). All combinations of inputs yielding the highest AUCs contained elastography features; four out of six combinations of inputs contained HK features; all combinations also contained B-mode gray level features. The Nakagami m-parameter was not selected in any input combination providing the highest AUC-ROC, likely because of its redundancy with HK features [53]. For the classification task of detecting a maximum lipid area $\geq$ 10%, different combinations of features provided similar AUC-ROC. For the task of detecting ruptured fibrous caps and vulnerable or neovascularized plaques, a combination without HK features was not statistically significantly different from the combination containing an HK feature. These results are in agreement with a preliminary version of this study where neural network classification based solely on elastograms yielded a specificity of 67% for a sensitivity of 83%; whereas with combined QUS features of different types, the specificity was raised to 79% for the same sensitivity [54].

The lowest AUCs were obtained in the case of detection of a maximum lipid area $\geq$ 10% (0.79 with 95% CI of 0.77–0.82), and identification of patients with symptomatic carotid artery plaque (0.83 with 95% CI of 0.81–0.84). For all other classification tasks, AUCs greater than 0.90 were obtained: 0.90 (95% CI of 0.80–0.92) for detecting a maximum lipid area $\geq$ 25%; 0.95 (95% CI of 0.94–0.96) for a maximum calcium area $\geq$ 10%; 0.97 (95% CI of 0.95–0.98) for a ruptured fibrous cap; and 0.91 (95% CI of 0.89–0.93) for identifying vulnerable or neovascularized carotid artery plaques.

The proposed method was able to detect a ruptured fibrous cap even if US imaging does not have the resolution to perform visually this task. Since an active inflammatory reaction is associated with ruptured plaques [55], we hypothesize that changes in plaque tissue microstructure and composition, which are related to ruptured fibrous caps, could be detected by the proposed machine learning classification method.

Carotid artery plaque characterization was also previously addressed with US imaging methods. Lipid core and calcium assessment was investigated with acoustic radiation force impulse US imaging, yielding AUCs of 0.89 and 0.86 for identification of soft and stiff plaque components, respectively [56]. Vulnerable and stable plaques were also classified, based on strain features, with an AUC of 0.85 [57]. In another study, (fibro)atheromatous plaques were distinguished from fibrous ones with an AUC of 0.80, also based on strain features [12]. Previously, we have used elastograms to identify vulnerable or neovascularized carotid artery plaques with an AUC value of 0.89 [27]; a lower AUC with elastography alone (the same parameters as in [24]) was obtained in this study (AUC = 0.86), but this may be explained by the lack of cross-validation in our previous report. We have also used US elastography and echogenicity combined with a principal components analysis (PCA), which allowed discriminating symptomatic versus asymptomatic patients with an AUC of 0.78 (with a single threshold classifier of the PCA variable) [30]. Better performance was obtained in the current report using the random forest classification algorithm (AUC = 0.83).

Machine learning algorithms have been used previously to predict stroke using echogenicity features of carotid artery plaques with an AUC of 0.80 [58] and to predict the evolution

of coronary artery plaque using intravascular US virtual histology with classification performance (G-mean) between 77% and 86% depending of the initial plaque types [59]. Both studies used support vector machine classification.

Imbalanced data sets in which one class is considerably outweighed may be associated with an overall acceptable accuracy, though with poor performance over the smallest class, by simply ignoring this class. Three tasks had imbalanced data sets: detection of a maximum lipid area $\geq$ 25% (7 out of 31); detection of a ruptured fibrous cap (5 out of 31); and identification of patients with symptomatic carotid artery plaque (26 out of 66). Precision-recall curve (PRC) was suggested as an alternative to ROC curve for classifier performance evaluation in the case of imbalanced data sets [60], [61]. PRC curves turned out to be the most informative tool to compare classifiers when the event rate is low [61]. PRC curves were thus computed for the three classification tasks with imbalanced data sets for all combinations of input features (data not shown). For task #2 in Table V (detection of a maximum lipid area $\geq$ 25%), the highest AUC-PRC were obtained for inputs Elasto + HK + echogenicity and Elasto + Nakagami + echogenicity (lines 1 and 2 in Table V). There was no statistically significant difference between the AUC-PRC of these two input combinations; AUC-PRC corresponding to lines 1 and 2 in Table V were 0.76 (95% CI 0.68–0.81) and 0.76 (95% CI 0.67–0.81), respectively. For task #4 (detection of a ruptured fibrous cap), the highest AUC-PRC was obtained with the input Elasto + HK + echogenicity (line 1); the HK + echogenicity features thus increased the AUC-PRC (0.88, 95% CI 0.79–0.91 compared to 0.82, 95% CI 0.72–0.86), while there was no added value to the AUC-ROC associated with this feature selection. For identification of patients with symptomatic carotid artery plaque (task #6), the highest AUC-PRC was similar to AUC-ROC (0.80, 95% CI 0.77–0.81); i.e., the combination of elastography, echogenicity, HK, or Nakagami features.

A. Study Limitations

In machine learning, large data sets usually ensure more reproducible results. In this study, results were based on populations of 31 and 66 patients. (We selected one carotid side per patient to avoid paired data.) Moreover, ruptured fibrous caps were observed in only five cases. Selected elastography and QUS features used for carotid artery plaque characterization could thus change if the proposed classification scheme is applied to a larger sample size. To improve the robustness of conclusion, the "0.632+" bootstrap method was selected and confidence intervals were provided. Adding additional samples would reduce these intervals but may not necessarily raise the classification performance. Nevertheless, to confirm the findings of this study, particularly in the case of imbalanced data sets, a larger study population would be necessary.

To conclude, this study has shown the advantage of using a machine learning strategy to combine different features from the same US acquisitions for the task of identifying carotid artery plaque components of vulnerability.

REFERENCES

[1] R. C. Pasternak *et al.*, "Atherosclerotic vascular disease conference writing group I: Epidemiology," *Circulation*, vol. 109, no. 21, pp. 2605–2612, 2004.

[2] W. Brinjikji, J. Huston, III, A. A. Rabinstein, G.-M. Kim, A. Lerman, and G. Lanzino, "Contemporary carotid imaging: From degree of stenosis to plaque vulnerability," *J. Neurosurg.*, vol. 124, no. 1, pp. 27–42, 2016.

[3] A. Millon *et al.*, "High-resolution magnetic resonance imaging of carotid atherosclerosis identifies vulnerable carotid plaques," *J. Vascular Surg.*, vol. 57, no. 4, pp. 1046–1051.e2, 2013.

[4] L. Esposito-Bauer *et al.*, "MRI plaque imaging detects carotid plaques with a high risk for future cerebrovascular events in asymptomatic patients," *PLoS ONE*, vol. 8, no. 7, p. e67927, 2013.

[5] W. S. Kerwin, Z. Miller, and C. Yuan, "Imaging of the high-risk carotid plaque: Magnetic resonance imaging," *Seminars Vascular Surg.*, vol. 30, no. 1, pp. 54–61, 2017.

[6] A. R. Naylor *et al.*, "Editor's choice—Management of atherosclerotic carotid and vertebral artery disease: 2017 clinical practice guidelines of the European society for vascular surgery (ESVS)," *Eur. J. Vascular Endovascular Surg.*, vol. 55, no. 1, pp. 3–81, 2018.

[7] J. L. Fleg *et al.*, "Detection of high-risk atherosclerotic plaque: Report of the NHLBI working group on current status and future directions," *JACC, Cardiovascular Imag.*, vol. 5, no. 9, pp. 941–955, 2012.

[8] H. Beaussier *et al.*, "Mechanical and structural characteristics of carotid plaques by combined analysis with echotracking system and MR imaging," *JACC, Cardiovascular Imag.*, vol. 4, no. 5, pp. 468–477, 2011.

[9] F. Liu, Q. Yong, Q. Zhang, P. Liu, and Y. Yang, "Real-time tissue elastography for the detection of vulnerable carotid plaques in patients undergoing endarterectomy: A pilot study," *Ultrasound Med. Biol.*, vol. 41, no. 3, pp. 705–712, Mar. 2015.

[10] X. Wang *et al.*, "Classification of symptomatic and asymptomatic patients with and without cognitive decline using non-invasive carotid plaque strain indices as biomarkers," *Ultrasound Med. Biol.*, vol. 42, no. 4, pp. 909–918, 2016.

[11] C. Huang *et al.*, "Non-invasive identification of vulnerable atherosclerotic plaques using texture analysis in ultrasound carotid elastography: An *in vivo* feasibility study validated by magnetic resonance imaging," *Ultrasound Med. Biol.*, vol. 43, no. 4, pp. 817–830, 2017.

[12] H. H. Hansen, G. J. de Borst, M. L. Bots, F. L. Moll, G. Pasterkamp, and C. L. de Korte, "Validation of noninvasive *in vivo* compound ultrasound strain imaging using histologic plaque vulnerability features," *Stroke*, vol. 47, no. 11, pp. 2770–2775, 2016.

[13] M. E. Boesen, D. Singh, B. K. Menon, and R. Frayne, "A systematic literature review of the effect of carotid atherosclerosis on local vessel stiffness and elasticity," *Atherosclerosis*, vol. 243, no. 1, pp. 211–222, 2015.

[14] M.-L. M. Grønholdt, B. G. Nordestgaard, T. V. Schroeder, S. Vorstrup, and H. Sillesen, "Ultrasonic echolucent carotid plaques predict future strokes," *Circulation*, vol. 104, no. 1, pp. 68–73, 2001.

[15] H. Hashimoto, M. Tagaya, H. Niki, and H. Etani, "Computer-assisted analysis of heterogeneity on B-mode imaging predicts instability of asymptomatic carotid plaque," *Cerebrovascular Diseases*, vol. 28, pp. 357–364, Sep. 2009.

[16] R. J. Doonan *et al.*, "Plaque echodensity and textural features are associated with histologic carotid plaque instability," *J. Vascular Surg.*, vol. 64, no. 3, pp. 671–677.e8, 2016.

[17] A. N. Nicolaides *et al.*, "Asymptomatic internal carotid artery stenosis and cerebrovascular risk stratification," *J. Vascular Surg.*, vol. 52, no. 6, pp. 1486–1496.e5, 2010.

[18] C. C. Mitchell *et al.*, "Histopathologic validation of grayscale carotid plaque characteristics related to plaque vulnerability," *Ultrasound Med. Biol.*, vol. 43, no. 1, pp. 129–137, 2017.

[19] A. Gupta *et al.*, "Plaque echolucency and stroke risk in asymptomatic carotid stenosis: A systematic review and meta-analysis," *Stroke*, vol. 46, pp. 91–97, Jan. 2015.

[20] J. E. Wilhjelm, M. L. Gronholdt, B. Wiebe, S. K. Jespersen, L. K. Hansen, and H. Sillesen, "Quantitative analysis of ultrasound B-mode images of carotid atherosclerotic plaque: Correlation with visual classification and histological examination," *IEEE Trans. Med. Imag.*, vol. 17, no. 6, pp. 910–922, Dec. 1998.

[21] J. C. R. Seabra, L. M. Pedro, J. F. e Fernandes, and J. M. Sanches, "A 3-D ultrasound-based framework to characterize the echo morphology of carotid plaques," *IEEE Trans. Biomed. Eng.*, vol. 56, no. 5, pp. 1442–1453, May 2009.

[22] J. C. R. Seabra and J. M. Sanches, "A 3D graph-cut based algorithm for evaluating carotid plaque echogenicity and texture," in *Recent Advances in Biomedical Engineering*. Rijeka, Croatia: InTech, 2009.

[23] P. M. Shankar, F. Forsberg, and L. Lown, "Statistical modeling of atherosclerotic plaque in carotid B mode images—A feasibility study," *Ultrasound Med. Biol.*, vol. 29, no. 9, pp. 1305–1309, 2003.

[24] M. Han, J. Wan, Y. Zhao, X. Zhou, and M. Wan, "Nakagami-*m* parametric imaging for atherosclerotic plaque characterization using the coarse-to-fine method," *Ultrasound Med. Biol.*, vol. 43, no. 6, pp. 1275–1289, 2017.

[25] X. Huang *et al.*, "Identification of ultrasonic echolucent carotid plaques using discrete Fréchet distance between bimodal gamma distributions," *IEEE Trans. Biomed. Eng.*, vol. 65, no. 5, pp. 949–955, May 2018.

[26] C. Naim *et al.*, "Characterisation of carotid plaques with ultrasound elastography: Feasibility and correlation with high-resolution magnetic resonance imaging," *Eur. Radiol.*, vol. 23, no. 7, pp. 2030–2041, 2013.

[27] M.-H. Roy Cardinal *et al.*, "Carotid artery plaque vulnerability assessment using noninvasive ultrasound elastography: Validation with MRI," *Amer. J. Roentgenol.*, vol. 209, no. 1, pp. 142–151, 2017.

[28] F. Destrempes, E. Franceschini, F. T. H. Yu, and G. Cloutier, "Unifying concepts of statistical and spectral quantitative ultrasound techniques," *IEEE Trans. Med. Imag.*, vol. 35, no. 2, pp. 488–500, Feb. 2016.

[29] I. Trop *et al.*, "The added value of statistical modeling of backscatter properties in the management of breast lesions at US," *Radiology*, vol. 275, no. 3, pp. 666–674, 2015.

[30] G. Cloutier, M. H. Roy Cardinal, Y. Ju, M.-F. Giroux, S. Lanthier, and G. Soulez, "Carotid plaque vulnerability assessment using ultrasound elastography and echogenicity analysis," *Amer. J. Roentgenol.*, to be published.

[31] F. Destrempes, J. Meunier, M.-F. Giroux, G. Soulez, and G. Cloutier, "Segmentation of plaques in sequences of ultrasonic B-mode images of carotid arteries based on motion estimation and a Bayesian model," *IEEE Trans. Biomed. Eng.*, vol. 58, no. 8, pp. 2202–2211, Aug. 2011.

[32] R. J. van der Geest *et al.*, "Advanced three-dimensional postprocessing in computed tomographic and magnetic resonance angiography," in *Cardiovascular Imaging*, V. Ho and G. Reddy, Eds. St. Louis, MO, USA: Elsevier, 2011, pp. 1128–1143.

[33] R. L. Maurice, M. Daronat, J. Ohayon, É. Stoyanova, F. S. Foster, and G. Cloutier, "Non-invasive high-frequency vascular ultrasound elastography," *Phys. Med. Biol.*, vol. 50, no. 7, pp. 1611–1628, 2005.

[34] E. Mercure *et al.*, "A compensative model for the angle-dependence of motion estimates in noninvasive vascular elastography," *Med. Phys.*, vol. 38, no. 2, pp. 727–735, 2011.

[35] J. Marroquin, S. Mitter, and T. Poggio, "Probabilistic solution of ill-posed problems in computational vision," *J. Amer. Stat. Assoc.*, vol. 82, no. 397, pp. 76–89, 1987.

[36] P. M. Shankar, "A general statistical model for ultrasonic backscattering from tissues," *IEEE Trans. Ultrason., Ferroelectr., Freq. Control*, vol. 47, no. 3, pp. 727–736, May 2000.

[37] F. Destrempes, J. Meunier, M.-F. Giroux, G. Soulez, and G. Cloutier, "Segmentation in ultrasonic B-mode images of healthy carotid arteries using mixtures of Nakagami distributions and stochastic optimization," *IEEE Trans. Med. Imag.*, vol. 28, no. 2, pp. 215–229, Feb. 2009.

[38] F. Destrempes, J. Porée, and G. Cloutier, "Estimation method of the homodyned K-distribution based on the mean intensity and two log-moments," *SIAM J. Imag. Sci.*, vol. 6, no. 3, pp. 1499–1530, 2013.

[39] V. Dutt and J. F. Greenleaf, "Ultrasound echo envelope analysis using a homodyned K distribution signal model," *Ultrason. Imag.*, vol. 16, no. 4, pp. 265–287, 1994.

[40] L. Breiman, "Random forests," *Mach. Learn.*, vol. 45, no. 1, pp. 5–32, 2001.

[41] T. K. Ho, "The random subspace method for constructing decision forests," *IEEE Trans. Pattern Anal. Mach. Intell.*, vol. 20, no. 8, pp. 832–844, Aug. 1998.

[42] A. Liaw and M. Wiener, "Classification and regression by randomforest," *R News*, vol. 2, no. 3, pp. 18–22, 2002.

[43] H. He and E. A. Garcia, "Learning from imbalanced data," *IEEE Trans. Knowl. Data Eng.*, vol. 21, no. 9, pp. 1263–1284, Sep. 2009.

[44] B. Efron and R. Tibshirani, "Improvements on cross-validation: The 632+ bootstrap method," *J. Amer. Stat. Assoc.*, vol. 92, no. 438, pp. 548–560, 1997.

[45] J. Friedman, T. Hastie, and R. Tibshirani, *The Elements of Statistical Learning* (Springer Series in Statistics), vol. 1. New York, NY, USA: Springer-Verlag, 2001.

[46] A. M. Molinaro, R. Simon, and R. M. Pfeiffer, "Prediction error estimation: A comparison of resampling methods," *Bioinformatics*, vol. 21, no. 15, pp. 3301–3307, 2005.

[47] E. R. DeLong, D. M. DeLong, and D. L. Clarke-Pearson, "Comparing the areas under two or more correlated receiver operating characteristic curves: A nonparametric approach," *Biometrics*, vol. 44, no. 3, pp. 837–845, 1988.

[48] I. Guyon and A. Elisseeff, "An introduction to variable and feature selection," *J. Mach. Learn. Res.*, vol. 3, pp. 1157–1182, Jan. 2003.

[49] A. Gupta *et al.*, "Carotid plaque MRI and stroke risk: A systematic review and meta-analysis," *Stroke*, vol. 44, no. 11, pp. 3071–3077, 2013.

[50] J. Sun *et al.*, "Carotid plaque lipid content and fibrous cap status predict systemic CV outcomes: The MRI substudy in AIM-HIGH," *JACC, Cardiovascular Imag.*, vol. 10, no. 3, pp. 241–249, 2017.

[51] K. R. Nandalur, A. D. Hardie, P. Raghavan, M. J. Schipper, E. Baskurt, and C. M. Kramer, "Composition of the stable carotid plaque," *Stroke*, vol. 38, no. 3, pp. 935–940, 2007.

[52] Q. J. van den Bouwhuijsen *et al.*, "Coexistence of calcification, intraplaque hemorrhage and lipid core within the asymptomatic atherosclerotic carotid plaque: The rotterdam study," *Cerebrovascular Diseases*, vol. 39, nos. 5–6, pp. 319–324, 2015.

[53] F. Destrempes and G. Cloutier, "A critical review and uniformized representation of statistical distributions modeling the ultrasound echo envelope," *Ultrasound Med. Biol.*, vol. 36, no. 7, pp. 1037–1051, 2010.

[54] M. H. Roy-Cardinal, F. Destrempes, G. Soulez, and G. Cloutier, "Homodyned K-distribution parametric maps combined with elastograms for carotid artery plaque assessment," in *Proc. IEEE Int. Ultrason. Symp. (IUS)*, Sep. 2016, pp. 1–4.

[55] A. C. van der Wal, A. E. Becker, C. M. van der Loos, and P. K. Das, "Site of intimal rupture or erosion of thrombosed coronary atherosclerotic plaques is characterized by an inflammatory process irrespective of the dominant plaque morphology," *Circulation*, vol. 89, pp. 36–44, Jan. 1994.

[56] T. J. Czernuszewicz *et al.*, "Performance of acoustic radiation force impulse ultrasound imaging for carotid plaque characterization with histologic validation," *J. Vascular Surg.*, vol. 66, no. 6, pp. 1749–1757.e3, 2017.

[57] C. Huang *et al.*, "Ultrasound-based carotid elastography for detection of vulnerable atherosclerotic plaques validated by magnetic resonance imaging," *Ultrasound Med. Biol.*, vol. 42, no. 2, pp. 365–377, 2016.

[58] E. C. Kyriacou *et al.*, "Prediction of high-risk asymptomatic carotid plaques based on ultrasonic image features," *IEEE Trans. Inf. Technol. Biomed.*, vol. 16, no. 5, pp. 966–973, Sep. 2012.

[59] L. Zhang, A. Wahle, Z. Chen, J. J. Lopez, T. Kovarnik, and M. Sonka, "Predicting locations of high-risk plaques in coronary arteries in patients receiving statin therapy," *IEEE Trans. Med. Imag.*, vol. 37, no. 1, pp. 151–161, Jan. 2018.

[60] J. Davis and M. Goadrich, "The relationship between precision-recall and ROC curves," in *Proc. 23rd Int. Conf. Mach. Learn.*, 2006, pp. 233–240.

[61] T. Saito and M. Rehmsmeier, "The precision-recall plot is more informative than the ROC plot when evaluating binary classifiers on imbalanced datasets," *PLoS ONE*, vol. 10, no. 3, p. e0118432, 2015.

Marie-Hélène Roy-Cardinal received the B.Eng. degree in computer engineering from the École Polytechnique of Montreal, Montreal, QC, Canada, in 2001, and the Ph.D. degree in biomedical engineering from the University of Montreal, Montreal, in 2008.

Since 2009, she has been a Research Associate with the Laboratory of Biorheology and Medical Ultrasonics, University of Montreal Hospital Research Center, Montreal. Her current research interests include intravascular ultrasound imaging, segmentation applied to ultrasound imaging, tissue characterization with ultrasound elastography and quantitative ultrasound, and machine learning applied to ultrasound imaging.

François Destrempes received the B.Sc. degree in mathematics from the University of Montreal, Montreal, QC, Canada, in 1985, the Ph.D. degree in mathematics from Cornell University, Ithaca, NY, USA, in 1990, and the Ph.D. degree in computer science from the University of Montreal in 2006.

He was a Post-Doctoral Fellow with the Centre de recherches mathématiques, University of Montreal from 1990 to 1992. He was a Lecturer at Concordia University, Montreal, and an Assistant Professor of mathematics at the University of Ottawa, Ottawa, ON, Canada, the University of Toronto, Toronto, ON, Canada, and the University of Alberta, Edmonton, AB, Canada. He was a Post-Doctoral Fellow at the Laboratory of Biorheology and Medical Ultrasonics, University of Montreal Hospital Research Center, Montreal. Since 2008, he has been a Research Associate with the Laboratory of Biorheology and Medical Ultrasonics, University of Montreal Hospital Research Center. He has authored or coauthored 33 articles and two book chapters. His current research interests include ultrasound imaging, segmentation of ultrasound imaging, quantitative ultrasound, and machine learning.

Gilles Soulez is currently a Vascular and Interventional Radiologist with the University of Montreal Hospital, Montreal, QC, Canada. He is a Professor of radiology and the Chair of the Department of Radiology, Radio-Oncology and Nuclear Medicine with the University of Montreal, Montreal. His research program conducted at the University of Montreal Hospital Research Center is exclusively dedicated to vascular and interventional radiology with a particular interest in the field of vascular ultrasound elastography to characterize vascular vulnerability, aneurysm endovascular repair, peripheral vascular disease, and advanced image guidance for interventional radiology procedures.

Guy Cloutier (S'89–M'90–SM'07) received the B.Eng. degree from the Université du Québec à Trois-Rivières, Trois-Rivières, QC, Canada, in 1984, and the M.Sc. and Ph.D. degrees from the École Polytechnique de Montréal, Montreal, QC, Canada, in 1986 and 1990, respectively.

From 1990 to 1992, he was a Post-Doctoral Fellow at The Pennsylvania State University, State College, PA, USA, with Prof. K. Kirk Shung. He is currently the Director of the Laboratory of Biorheology and Medical Ultrasonics with the University of Montreal Hospital Research Center (www.lbum-crchum.com), Montreal, a Professor with the Department of Radiology, Radio-Oncology and Nuclear Medicine, and a member of the Institute of Biomedical Engineering with the University of Montreal, Montreal. He has authored close to 200 peer-reviewed articles in these fields and holds 10 active patents. His research interests are in quantitative ultrasound imaging, quasi-static and dynamic ultrasound elastography, development of multiphysics imaging methods, and biomechanical modeling.

Dr. Cloutier licensed three technologies and was a recipient of the National Scientist Award of the Fonds de la Recherche en Santé du Québec from 2004 to 2009. He is an Associate Editor of the IEEE TRANSACTIONS ON ULTRASONICS, FERROELECTRICS, AND FREQUENCY CONTROL and *Plos One*, an Invited Associate Editor of *Medical Physics*, and a member of the editorial board of *Current Medical Imaging Reviews*, and was a member of the international advisory editorial board of *Ultrasound in Medicine and Biology* for 15 years.